

# A Light-Switchable Liquid Metamaterial Mirror

Sean Cormier, Andrew R. Salmon, Dean Kos, and Jeremy J. Baumberg\*

A metamaterial film composed of gold nanoparticles wrapped in thin thermoresponsive polymer shells is described. The nanoparticle shells are kept partially hydrated so that the film acts as a “liquid mirror” and shows subtle interactions due to its composite metamaterial nature. Optically heating the film collapses the polymer, increasing the gold fill fraction and raising the reflectivity. This in turn decreases the optothermal absorption, making both the reflectivity and optothermal absorption nonlinear. When the polymer collapses, the film buckles due to thermophoretic flows competing against surface tension. These interactions generate a remarkable array of dynamic behaviors. Exposing the films to light causes an insulator-to-metal transition. Defects can be healed by returning the film to the liquid phase. Laser illumination of micrometer-scale regions generates local dimples at low power and sinters microscale tracks at high power. When microbeads are combined into these films, optical switching results in quenching of their photoluminescence as well as the ability to manipulate their spatial position in real time.

## 1. Introduction

Metamaterials have been of considerable interest across the entire electromagnetic spectrum for cloaking objects,<sup>[1]</sup> modifying scattering signatures,<sup>[2]</sup> near-field focusing metalenses,<sup>[3]</sup> enhancing emitters and absorbers,<sup>[4,5]</sup> and a host of other capabilities. In recent years, interest has progressed from static systems to creating active metamaterials and metadevices, often using optical nonlinearities in order to switch light using light.<sup>[6]</sup> For example, active metamaterials have been used for beam steering in lidar and tunable metalenses.<sup>[6,7]</sup> However such systems use lithographic techniques which suffer a trade-off between expense, resolution, and device area.<sup>[8]</sup> One simple bottom-up approach would be to use the large optical nonlinearities of metal solid–liquid phase transitions thus avoiding the need for patterning (for instance in Au<sup>[9]</sup> or Ga<sup>[10]</sup>); however, the large lateral heat conductivity of metals leads to switching

of large sample areas unless pixilation is imposed and maintained.

Here, we use an alternative approach for optically nonlinear active metamaterials. We assemble metamaterial elements composed of  $D = 15$  nm diameter spherical Au NPs with 5 nm poly(*N*-isopropylacrylamide) (pNIPAM) coatings into random close-packed films (see Section 5). The volume defined by an optical wavelength thus encloses  $>10^4$  NPs, thus truly accessing the metamaterial regime. The pNIPAM thermoresponsive polymer has a lower critical solution temperature at  $T_c = 32$  °C.<sup>[11]</sup> Below this temperature the polymer is swollen by water, whereas for  $T > T_c$  it expels the water and collapses its volume by up to a factor of 10. Previously, we showed that the unusually high nanonewton forces produced are sufficient to overcome van der Waals

attractions between metal nanoparticles, thus allowing reversible disassembly of aggregates.<sup>[12]</sup> By now concentrating these actuating nanotransducer (ANT) nanoparticles so that excess water is removed (see Section 5), we can cast the nanoparticles into a thin film (formed of a dense metallic liquid slurry) on porous alumina substrates (Figure 1a shows the cross-section of a dried film). This substrate separates the “liquid metal” film from a water reservoir, allowing for water to be supplied to the film without washing it away. The film osmotic pressure determines the extent of hydration, and this varies depending on the pNIPAM phase. Heating the film above  $T_c$  (either directly or with light) drives water across the alumina membrane, collapsing the film thickness (Figure 1b). We term this a liquid metamaterial mirror (LMM) because it flows like a liquid in the cool state, is highly reflective, and has dynamic metamaterial properties.

In this paper, a range of light-induced functionalities based on this promising LMM system are reported. Light-induced switching causes local curvature to give microdimples that focus light and which can be translated around at high speed. We also show that these films can heal around defects and can be used to write conducting tracks. When they are employed to support colloidal microbeads, a range of effects including quenching and manipulation can also be induced. This system thus forms a new type of active metamaterial whose optical nonlinearities are capable of many functionalities.

The optical properties of such films under large area thermal heating have been previously reported by us,<sup>[13]</sup> showing a metal-insulator transition in the green-red region of the visible spectrum (Figure 1b,c) as the metal fraction of the film changes from  $f = 35$  to 50% when it expels water and the pNIPAM coatings collapse. Using an approximate composite

Dr. S. Cormier, Dr. A. R. Salmon, Dr. D. Kos, Prof. J. J. Baumberg  
Nanophotonics Centre  
Cavendish Laboratory  
University of Cambridge  
Cambridge CB3 0HE, UK  
E-mail: jjb12@cam.ac.uk

 The ORCID identification number(s) for the author(s) of this article can be found under <https://doi.org/10.1002/adom.202000396>.

© 2020 The Authors. Published by WILEY-VCH Verlag GmbH & Co. KGaA, Weinheim. This is an open access article under the terms of the Creative Commons Attribution License, which permits use, distribution and reproduction in any medium, provided the original work is properly cited.

DOI: 10.1002/adom.202000396

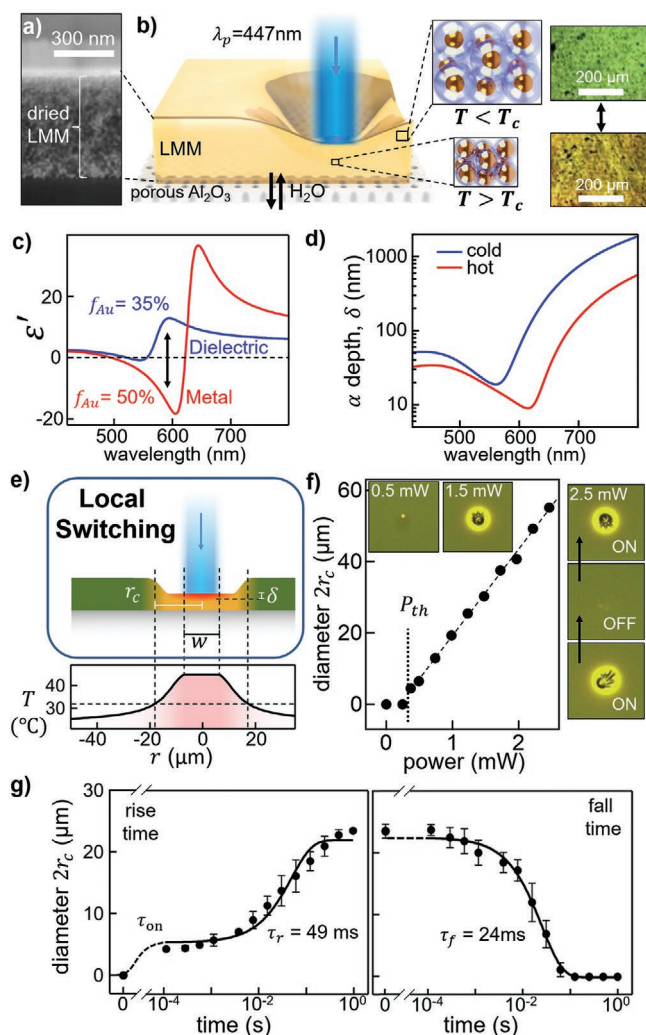


**Figure 1.** Local optical switching of liquid metamaterial mirror (LMM). a) Cross-section of dried LMM composed of 15 nm Au nanoparticles coated with thin thermoresponsive polymer shell. b) Schematic of light-induced local deformation of LMM, with images and structure for hot and cold states. c) Effective real permittivity of LMMs above and below  $T_c$ , and d) corresponding absorption depth for light incident onto LMM film. e) Schematic showing switched region around irradiation spot, with temperature distribution. f) Diameter of switched area versus irradiation power. Laser spot  $w = 4 \mu\text{m}$ ,  $\lambda_p = 447 \text{ nm}$ . Insets show images of LMM with laser filtered out (right side) reversible switching. g) Diameter of switched area versus time after irradiation switched on and off. Diameters measured from time-stamped frames captured with a high-speed camera.

Maxwell-Garnett model,<sup>[13]</sup> we can derive the real and imaginary refractive index in each state (cold  $<T_c$  and hot  $>T_c$ ), as well as the absorption depth of the film at different wavelengths (Figure 1d). These both show how the effective plasma frequency of this metamaterial red-shifts when the gold fill fraction increases. The film volume change can be estimated from this extracted gold fill fraction, depending on the ratio  $f_{\text{cold}}/f_{\text{hot}}$ . From this we estimate a volume change by a factor of 0.7. We observed no change in film area, so this corresponds to a thickness change by the same factor.

The change in absorption depth, which can be more than an order of magnitude, gives subtle nonlinear properties.

Irradiation with 633 nm light which is off-resonant at room temperature allows light to penetrate through the entire film. As soon as this light triggers the switching at  $T_c$ , however, the absorption depth drops to  $\delta < 20 \text{ nm}$  so that only the very top layer of the film is now optically heated. This produces a complex interplay of feedback between the local thickness of the switched region and the heat transport (see below).

## 2. Results

Focusing a  $\lambda_p = 447 \text{ nm}$  laser to a  $4 \mu\text{m}$  spot using a  $20\times$  objective heats the upper 40 nm of the film (at  $\lambda_p$ ,  $\delta$  changes little with temperature; Figure 1d). Using a 447 nm laser allows us to efficiently filter out the laser for simultaneous optical imaging and spectroscopy. Switching requires a threshold power  $P_c \approx 0.3 \text{ mW}$  (Figure 1e,f), varying by  $<10\%$  across the sample. Above  $P_c$ , the observed diameter of the disk region of the film that switches (which has a sharply defined boundary of width less than our optical resolution) increases linearly with incident power. Biasing the sample at this transition (with heat or light), results in a very large optical nonlinearity (as for Ga/fiber devices<sup>[14]</sup>) that can be exploited for devices such as all-optical processors.

A simple model of this observed disk requires understanding of the composite thermal properties of this metamaterial. In the initial state (modeled as a thin film with radial outflow of heat), the central temperature rise from a laser of power  $P$  focused to a spot of radius  $w$  is

$$\Delta T = 2(2\pi)^{-3/2} \cdot \frac{aP}{\bar{\kappa} w} \quad (1)$$

where  $a \approx 0.85$  is the intensity fraction absorbed in the film (from the measured reflectivity of 0.15 at 447 nm) and  $\bar{\kappa}$  is the effective heat conductivity. The thermal conduction depends on the metal volume fill fraction  $f$ , and the thermal conductivity of both the pNIPAM shell  $\kappa_s = 0.6 \text{ W m}^{-1} \text{ K}^{-1}$  (assumed to be that of water of which it is  $>97\%$  by mass) and the Au core  $\kappa_c = 314 \text{ W m}^{-1} \text{ K}^{-1}$ . For close-packed metal spheres in a lower heat conducting matrix,<sup>[15]</sup> the effective conductivity

$$\bar{\kappa} = \kappa_s \left[ \frac{1 + 1.5f}{1 - f(1 + 0.9f)} \right] \quad (2)$$

varying from  $\kappa_s$  up to  $6\kappa_s$  as the fill fraction approaches 50% (although this model fails at large  $f$ ).

Using the resulting  $\bar{\kappa} = 5\kappa_s$ , with the required heating from room temperature of  $\Delta T_c = 12 \text{ K}$  to reach  $T_c$ , the diffraction-limited focused spot is predicted to give  $P_c = 0.2 \text{ mW}$ , which matches well the threshold power observed experimentally. Either using additional thermal biasing closer to  $T_c$ , or variants of pNIPAM with lower  $T_c$ <sup>[16]</sup> will allow this critical power to be at least tenfold reduced. For higher powers, the film heating profile is given by (Figure 1e)

$$\Delta T(r) = \frac{aP}{2\pi\bar{\kappa}r} \text{erf}\left(\frac{r}{\sqrt{2}w}\right) \quad (3)$$

so that well above the threshold, the radius of the switched region  $r_c = aP / (2\pi\bar{\kappa} \Delta T_c) = 1.3w(P/P_c)$ . This increases as

$8 \mu\text{m mW}^{-1}$  which well matches the experimental gradient (Figure 1f, dashed).

The pNIPAM thickness changes upon switching as  $d(f)$ , with the heat flow also sensitive to the separation of the metal cores  $2d$ . The increase in metal fill fraction thus increases the thermal conductivity, however models for  $\bar{\kappa}$  are not well tested in this near-touching limit. Our thermal metamaterial is in an interesting regime, since the thermal diffusion length around the heated metallic spheres (heat capacity at constant volume  $C_{\text{Au}}$  in water ( $C_{\text{H}_2\text{O}}$ ) is given by<sup>[17]</sup>  $l_d = \frac{1}{6} DC_{\text{Au}} / C_{\text{H}_2\text{O}} \approx 1.5 \text{ nm}$ , similar to the gap between spheres. Upon switching, the core separation  $2d$  reduces from 4.5 to 2.2 nm thus approaching a different thermal conduction regime, suggesting that the temperature distribution within the switched region is not as in the simple model shown in Figure 1e. We note that surface radiation is minimal for temperatures considered here, and that convection of water encapsulated by the pNIPAM is likely to be minimal, although nanoparticle flows are important (see below). A further complication are vertical thermal gradients below the laser spot. While excitation at 633 nm requires similar laser thresholds, the absorption depth reduces 30-fold on switching. These features suggest a more complex model, based on full finite element nonlinear modeling is required to fully investigate this intriguing switchable thermal metamaterial.

The composite thermal diffusivity should also control the response speed in these LMM films. We find that the initial turn-on transition is too rapid to observe ( $<100 \mu\text{s}$ ) as it is smeared out by the finite laser spot size. The initial disk size remains close to the laser spot diameter for 10 ms, before then increasing to its final value (here  $r_c = 11 \mu\text{m}$ ) with a rise time of 49 ms (Figure 1g). The fall time is found to be about twice as fast. For typical polymers and pNIPAM at room temperature, the expected  $\tau^D \sim r_c^2 / (4D)$  would give  $100 \mu\text{s}$  rise times, almost a 1000-fold faster than observed. One origin of this highly retarded heat conduction can be the enhanced specific heat capacity of pNIPAM which possesses a resonance at  $T_c$ .<sup>[18]</sup> However we suggest the more likely origin of this effect is in heat transport through thermophoretic flow of the nanoparticles at the edge of the switched region (Figure S7, Supporting Information). In this case, the heat transport would occur on times  $\tau^T \sim r_c^2 / (D^T \cdot \Delta T)$ , where  $D^T$  is the thermophoretic mobility measured as  $10^{-11} \text{ m}^2 \text{ s}^{-1} \text{ K}^{-1}$  for 100 nm pNIPAM microgel particles,<sup>[19]</sup> giving 100 ms timescales matching our observations.

This implies that switching speed under the laser spot itself is sub  $100 \mu\text{s}$ , but that the direct diffusion of heat outside this spot is surprisingly slow, with  $D < 10^{-9} \text{ m}^2 \text{ s}^{-1}$ , a 100-fold slower than in typical polymers. Because the thermal length is similar to the thickness of pNIPAM, and the Kapitza resistances at the Au/polymer interfaces are not understood, this heat transport regime is anomalous. Instead, thermal transport outside the optically pumped region is provided by thermophoretic transport of the ANTs on slower timescales. This provides better buffering between different spatial regions on the LMM films, reducing cross-talk. It also allows the microdimple to be translated around high speeds by deflecting the laser beam, to sculpt the surface of this LMM mirror in real time.

To determine the shape of the locally switched region is not straightforward. Traditional surface profiling is not useful since it must not block the optical excitation beam (hence

precluding environmental AFM or SEM), and has to operate at  $20\text{--}40 \text{ }^\circ\text{C}$  in aqueous environments without obstructing the porous underlayer acting as the reservoir. The high fill fraction LMM films are optical opaque as is the porous underlayer, hence simple transmission is not viable. We note first that the microdimple white-light reflection images show a central spot at the dimple center surrounded by a bright ring (Figure 1f; Figure S3a, Supporting Information),<sup>[20]</sup> corresponding to the switched region of higher reflectivity.

In order to locally measure the surface topology of the LMM we use differential-interference contrast in reflection (Figures S3 and S4, Supporting Information). Using this on light-induced LMM microdimples shows they are far from hemispherical in shape. A rapid drop in thickness is seen at the transition edge, with upward tilting just outside this perimeter, and upward dimpling in the central region. These results are consistent at different positions across the film, though the exact shape of the central region varies and can display hysteresis (see Figure 1f, right). This suggests a complex balance of thermophoretic forces and surface tension at the sharp circular interface between switched and nonswitched regions, with buckling into corrugations in the collapsed dimple floor (Figure S5, Supporting Information) related to the thermal metamaterial heat transport.

### 3. Discussion

The liquid metamaterial films display self-healing properties. If a hot switched film (using broad area white illumination) is scored with a blade, then temperature cycling from above to below  $T_c$  allows it to liquefy and surface tension to close this gap. This restores the original film surface again when switched back by illuminating to heat above  $T_c$  (Figure 2a,b). We note that texture observed on the film surface comes from

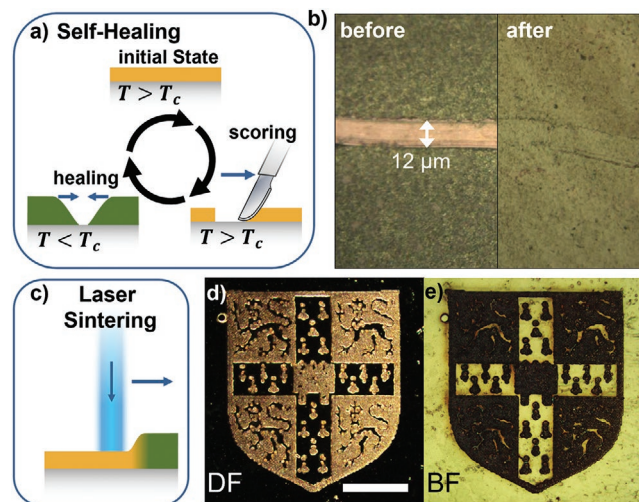


**Figure 2.** Self-healing and local gold opto-sintering of LMMs. a) Schematic of LMM healing by temperature cycling after scoring with a scalpel. b) Images of scored dry LMM film before and after temperature cycling using white light. c) Schematic of light-induced sintering at the laser spot using 447 nm irradiation. d) Dark-field and e) bright-field images of a sinter-written University logo, laser spot size is  $4 \mu\text{m}$ , and scale bar is  $100 \mu\text{m}$ . Laser power is  $9.8 \text{ mW}$ ,  $\approx 10\%$  above the sintering threshold.

the underlying porous alumina substrate (Figure S4d, Supporting Information). Such metamaterial self-healing makes these systems much more resilient to defects and damage than typical lithographically fashioned metamaterials.

Further increasing the laser power can decompose the pNIPAM coatings, resulting in irreversible nanoparticle sintering (Figure 2c–e). This can be used to write conducting tracks, and other persistent features in the LMM films. At these laser powers the switched region is >100  $\mu\text{m}$  diameter; however, the sintering only takes place under the laser spot, again confirming the surprisingly high thermal insulation of the LMMs and suggesting that the sintering is UV triggered and not thermally triggered. Hence this allows micrometer-scale metallic features to be written using such LMMs as a metallic liquid precursor resist.

The high mass density of these “metametal” films leads to their supporting colloids floating on top. A new functionality is observed when the LMM around such colloids is switched. We first use 1  $\mu\text{m}$  diameter dye-impregnated polystyrene spheres, and image their emission under blue illumination (Figure 3a,b). When the entire LMM is heated just above  $T_c$ , the emission completely disappears, but reappears immediately as the temperature is reduced below  $T_c$ . To understand this in more detail, we observe a single floating 30  $\mu\text{m}$   $\text{SiO}_2$  colloid as the LMM is locally switched using focused 447 nm laser light

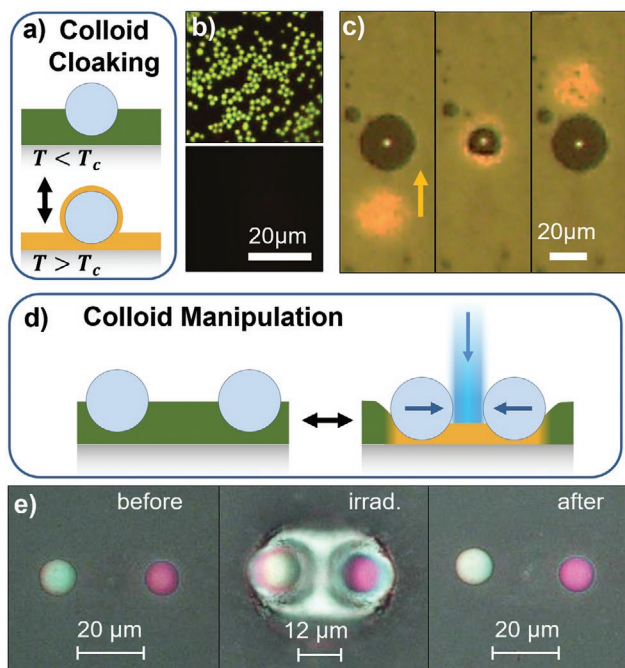


**Figure 3.** Optical cloaking and manipulation of interface colloids. a) Schematic of LMM film cloaking polymer colloids upon switching. b) Image of 1  $\mu\text{m}$  fluorescent polystyrene colloids (see materials) cloaked at the LMM surface using bulk heating, imaging luminescence ( $\lambda > 520$  nm) under broad area blue excitation (470–490 nm). c) Single 30  $\mu\text{m}$   $\text{SiO}_2$  colloid cloaked by scanning the focused 447 nm laser spot across the floating colloid (orange spot shows switched region). d) Schematic of light-induced manipulation of floating transparent colloids on LMM films. e) Sequential images of 10  $\mu\text{m}$  glass colloids brought closer together under optical forces induced by irradiating region between the particles with focused 447 nm irradiation of 0.9 mW.

(Figure 3c). The switched zone under the laser (appearing orange in the images) gives a dramatic reduction in the visible area of the floating colloid in reflection. This apparent size reduces, because the switched LMM now wets the glass sphere surface when it becomes hydrophobic, cloaking the colloid from view. This is a completely reversible effect (see Video S1 in the Supporting Information), allowing light-induced wetting and dewetting of objects to be rapidly switched.

The forces produced depend on the colloids involved, and can be used to manipulate their separation. With pairs of transparent  $\text{SiO}_2$  10  $\mu\text{m}$  spheres, switching the region in between them draws them closer together (Figure 3d,e). The sphere colors seen are produced by interference from reflections at the top/bottom glass surfaces and vary because the spheres have slightly different diameters. A 40% reduction in spacing between the spheres occurs rapidly (Figure 1g), but is restored when the laser is switched off. Again, a complex interplay of forces is evident in these dynamics, but shows the ability to move entrained objects around on top of the films at high speeds.

Finally, we note that the electrical properties of the LMM films also change upon illumination. Their dc resistance measured using two-terminal Au contacts underneath the film decreases by tenfold upon transiently switching the metamaterials (Figure S6, Supporting Information). This might be expected from an electron tunneling mechanism between the Au cores, but requires further investigation since ionic transport can also be involved, as well as local changes around the contact fingers.

## 4. Conclusion

We believe this robust metamaterial formulation, which is easily scalable, low-cost, and can be stored for months without degradation, offers a wide route to applications as well as providing an unusual platform for exploring switchable metamaterials properties in the optical, thermal, electrical, wetting, surface tension, and thermophoretic domains. The dense LMMs can also be packaged into microdroplets for long-term functionality,<sup>[21]</sup> and are benign, water solvated, and biocompatible so could be intriguing for light-tunable cellular substrates. A range of nanoparticle diameters can be used (as previously their switching was demonstrated in solution<sup>[12,13]</sup>); however, larger nanoparticles have a higher thermal conductivity and thus require larger laser powers for switching. The thermophoretic flows will be more complex at these higher metal fill fractions, while the switching spot size will reduce, suggesting an interesting domain of future study.

## 5. Materials and Fabrication

**Scalable Mirror Construction:** Liquid mirrors are composed of a layer of core–shell actuating nanotransducers (ANTs) composed of gold nanoparticles (15 nm diameter) coated with a pNIPAM polymer shell.

To synthesize ANTs a 200 mL aqueous solution  $2.5 \times 10^{-3}$  M in  $\text{HAuCl}_4$  and  $7.7 \times 10^{-3}$  M in  $\text{NaOH}$  was prepared. This solution was heated to 85  $^\circ\text{C}$  under reflux and then trisodium citrate was

injected to a final concentration of  $5 \times 10^{-3}$  M. After 20 min the resulting AuNP suspension was allowed to cool. The particles were measured to be  $15 \pm 2$  nm (standard deviation) from 50 TEM measurements. The particle concentration was measured to be  $1.8 \times 10^{13}$  mL<sup>-1</sup> by extinction spectroscopy. pNIPAM was coupled to the particle surface by ligand exchange: 4 mL of a 0.1 mg mL<sup>-1</sup> aqueous solution of amine-terminated pNIPAM (5.5 kDa, Merck) was added to 32 mL of the AuNP suspension. This mixture was heated to 40 °C and 4 mL of a 1 mg mL<sup>-1</sup> solution of the pNIPAM was added. The resulting suspension was cooled to room temperature to give the ANTs. These particles were concentrated by centrifugation and resuspended in the supernatant to 10<sup>14</sup> mL<sup>-1</sup>.

To form films, 10 µL of this concentrated ANT suspension was placed on a porous Al<sub>2</sub>O<sub>3</sub> membrane (Whatman Anodisc 25, 0.02 µm pores) and the excess water was allowed to evaporate. The membrane separates the film from a water reservoir which is free to diffuse into and out of the  $t = 100$  nm thick ANT film deposited on top. The bulk gold fill fraction  $f$  is 6% (cold)/10% (hot) while the top 50 nm of the film has a higher gold fill fraction that is 35% (cold)/50% (hot).

**Optical Imaging:** A modified Olympus BX51 microscope was used for imaging and optical spectroscopy. For microspectroscopy a 50 µm core optical fiber was coupled in a conjugate focal plane and attached to a spectrometer (Ocean Optics QE Pro) such that spectra could be taken from well-defined spatial regions of the image. Spectra were normalized by a silver mirror. For fluorescence imaging a fluorescence filter cube was used (Olympus U-MNB2). A fiber coupled 447 nm CW laser was used for local film switching.

**Microbead Cloaking:** For the fluorescent microbeads in Figure 3b, we use 1 µm diameter dye-doped polystyrene spheres with amine coating (Merck L9654). For the larger SiO<sub>2</sub> spheres that are uncoated (Merck 440345), we select different diameters under the microscope for Figure 3c,e.

## Supporting Information

Supporting Information is available from the Wiley Online Library or from the author. Online data is available at: <https://doi.org/10.17863/CAM.52821>

## Acknowledgements

The authors acknowledge EPSRC grants EP/N016920/1, EP/L027151/1, and NanoDTC EP/L015978/1 and EP/S005889/1. We thank V. Valev and T. Ding for previous discussions.

## Conflict of Interest

The authors declare no conflict of interest.

## Author Contributions

S.C., A.R.S., D.K., and J.J.B. devised the experimental techniques and developed sample fabrication; S.C. and J.J.B. developed the spectral analysis and analytic models; and all authors contributed in writing the manuscript.

## Keywords

gold nanoparticles, metafilms, metamaterials, optical nonlinearity, thermoresponsive

Received: March 6, 2020

Revised: May 14, 2020

Published online:

- [1] J. B. Pendry, D. Schurig, D. R. Smith, *Science* **2006**, *312*, 1780.
- [2] Z. Ruan, S. Fan, *Phys. Rev. Lett.* **2010**, *105*, 013901.
- [3] M. Khorasaninejad, F. Capasso, *Science* **2017**, *358*, eaam8100.
- [4] A. Poddubny, I. Iorsh, P. Belov, Y. Kivshar, *Nat. Photonics* **2013**, *7*, 948.
- [5] M. Esfandyarpour, E. C. Garnett, Y. Cui, M. D. McGehee, M. L. Brongersma, *Nat. Nanotechnol.* **2014**, *9*, 542.
- [6] N. I. Zheludev, Y. S. Kivshar, *Nat. Mater.* **2012**, *11*, 917.
- [7] A. M. Shaltout, V. M. Shalae, M. L. Brongersma, *Science* **2019**, *364*, eaat3100.
- [8] W. Qiao, W. Huang, Y. Liu, X. Li, L. Sen Chen, J. X. Tang, *Adv. Mater.* **2016**, *28*, 10353.
- [9] M. Brückner, J. H. Schäfer, C. Schiffer, J. Uhlenbusch, *J. Appl. Phys.* **1991**, *70*, 1642.
- [10] B. F. Soares, F. Jonsson, N. I. Zheludev, *Phys. Rev. Lett.* **2007**, *98*, 153905.
- [11] S. Lanza, E. Armelin, *Gels* **2017**, *3*, 36.
- [12] T. Ding, V. K. Valev, A. R. Salmon, C. J. Forman, S. K. Smoukov, O. A. Scherman, D. Frenkel, J. J. Baumberg, *Proc. Natl. Acad. Sci. USA* **2016**, *113*, 5503.
- [13] S. Cormier, T. Ding, V. Turek, J. J. Baumberg, *Adv. Opt. Mater.* **2018**, *6*, 1701281.
- [14] B. F. Soares, K. F. MacDonald, V. A. Fedotov, N. I. Zheludev, *Nano Lett.* **2005**, *5*, 2104.
- [15] D. Kumlutaş, I. H. Tavman, M. Turhan Çoban, *Compos. Sci. Technol.* **2003**, *63*, 113.
- [16] K. Jain, R. Vedarajan, M. Watanabe, M. Ishikiriya, N. Matsumi, *Polym. Chem.* **2015**, *6*, 6819.
- [17] O. M. Wilson, X. Hu, D. G. Cahill, P. V. Braun, *Phys. Rev. B* **2002**, *66*, 2243011.
- [18] I. Bischofberger, D. C. E. Calzolari, P. De Los Rios, I. Jelezarov, V. Trappe, *Sci. Rep.* **2014**, *4*, 4377.
- [19] S. Wongsuwarn, D. Vigolo, R. Cerbino, A. M. Howe, A. Vailati, R. Piazza, P. Cicutta, *Soft Matter* **2012**, *8*, 5857.
- [20] S. Coyle, G. V. Prakash, J. J. Baumberg, M. Abdelsalem, P. N. Bartlett, *Appl. Phys. Lett.* **2003**, *83*, 767.
- [21] A. R. Salmon, S. Cormier, W. Wang, C. Abell, J. J. Baumberg, *Adv. Opt. Mater.* **2019**, *7*, 1900951.